ACS OMEGA

http://pubs.acs.org/journal/acsodf

Article

Microwave-Assisted Synthesis of Bi_2S_3 and Sb_2S_3 Nanoparticles and Their Photoelectrochemical Properties

Mathato P. Motaung, Damian C. Onwudiwe,* and Wei Lei

Cite This: *ACS Omega* 2021, 6, 18975−18987

Read Online

ACCESS | Metrics & More | Article Recommendations

ABSTRACT: Bi_2S_3 and Sb_2S_3 nanoparticles were prepared by microwave irradiation of single-source precursor complexes in the presence of ethylene glycol as a coordinating solvent. The as-synthesized nanoparticles were characterized by X-ray diffraction (XRD), transmission electron microscopy (TEM), scanning electron microscopy (SEM) coupled with energy-dispersive X-ray (EDX), photoluminescence (PL), and UV−vis near-infrared (NIR) spectroscopy. Their electrochemical potential was examined in $[Fe(CN)]^{4-}/[Fe(CN)]^{3-}$ by cyclic and square wave voltammetry (CV and SWV) and electrochemical impedance spectroscopy (EIS). $GCEBi_2S_3$ and $GCESb_2S_3$ exhibit promising electrochemical performance and a higher specific capacitance of about 700−800 F/g in $[Fe(CN)]^{4-}/[Fe(CN)]^{3}$. Thin films of Bi_2S_3 and Sb_2S_3 were successfully incorporated in the fabrication of solar cell devices. The fabricated device using Bi_2S_3 (under 100 mW/cm^2) showed a power conversion efficiency (PCE) of 0.39%, with a V_{oc} of 0.96 V, a J_{sc} of 0.00228 mA/cm^2, and an FF of 44%. In addition, the device exhibits nonlinear current density−voltage characteristics, indicating that Bi_2S_3 was experiencing a Schottky contact. The Sb_2S_3-based solar cell device showed no connection in the dark and under illumination. Therefore, no efficiency was recorded for the device using Sb_2S_3, which indicated the ohmic nature of the film. This might be due to the current leakage caused by poor coverage. The nanoparticles were found to induce similar responses to the conventional semiconductor nanomaterials in relation to photoelectrochemistry. The present study indicates that Bi_2S_3 and Sb_2S_3 nanoparticles are promising semiconductor materials for developing optoelectronic and electrochemical devices as the films experience Schottky and Ohmic contacts.

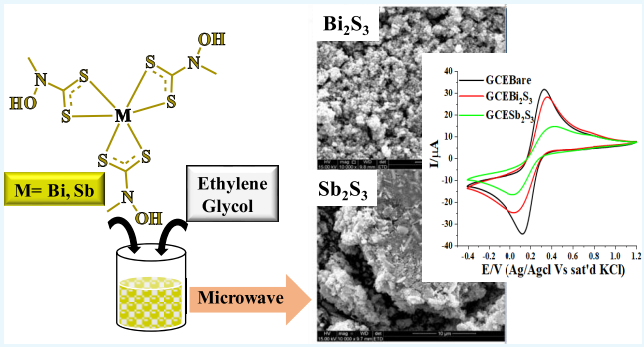

1. INTRODUCTION

Binary metal chalcogenides of the type A_2B_3 (A = As, Sb, Bi; B = S, Se, Te) have recently attracted great attention due to their unique optical and electronic properties.[1,2] Amongst the metal chalcogenides, metal sulfide nanoparticles are widely known for their potential application as energy conversion materials.[3,4] Sulfides such as Bi_2S_3 and Sb_2S_3 are one of the most important V−VI semiconductor nanoparticles and have great prospects in photocatalysis, light-emitting diodes, solar cell devices, biomedical probes, laser materials, photoluminescence (PL), and optoelectronic materials.[5,6] Both semiconductors have an orthorhombic system, which could be considered as an appropriate candidate for electrochemical and photovoltaic applications owing to their suitable optical properties such as band gaps (1.3 eV for Bi_2S_3 and 1.74 eV for Sb_2S_3), high stability, and absorption coefficients.[7,8] The low band gap, good ion conductivity, and redox chemistry character of these nanoparticles have made them attractive materials for various applications in a wide range of solar energy spectrum. In addition, they both have high photosensitivity, nontoxic nature, low cost, and their environmental friendliness make them superior materials compared to other semiconductors such as CdS and PbS[9,10] from the application point of view.

In the past few decades, metal sulfide-based solar cells have emerged as the most promising alternative for photovoltaic application.[11,12] Some metal sulfides have improved electronic conductivities than their oxide counterparts due to the lower electronegativity of sulfur compared to that of oxygen, which exhibit electron affinity and act as electron traps in the structure of the nanoparticles.[13] Sulfur vacancy in metal sulfides supports the formation of defect band transition above the valence band of nanoparticles, which provides a promising platform for the transfer of carriers from the UV/vis to near-infrared range of the solar spectrum.[14−16] Due to defects and charge traps within the band gap of metal sulfides, electrons/

Received: April 30, 2021
Accepted: June 30, 2021
Published: July 13, 2021

holes could result in enhanced carrier Coulombic coupling.[17] However, surplus electron/hole pairs are excited by the absorbed excess energy to improve photoelectric sensitivity and photocurrent capability of the material.[18,19]

Several methods such as thermal decomposition, hydrothermal/solvothermal, biomolecule-assisted pathways, and microwave irradiation have been developed for the synthesis of metal sulfides, which have several application advantages in electrochemical supercapacitors.[20−22] The use of ethylene glycol as a solvent in solvothermal synthesis has been widely reported.[23] It is a hydrophilic liquid, which is water-soluble, and also a biocompatible organic solvent. Due to its high polarizability, it is an excellent microwave-absorbing agent, thereby resulting in a characteristic high heating rate and considerably shortened reaction time.[24,25] In this study, we report the preparation of Bi_2S_3 and Sb_2S_3 nanoparticles through a microwave irradiation technique using ethylene glycol as both a solvent and a capping agent; and *N*-methyl-*N*-ethanoldithiocarbamate complexes of Bi(III) and Sb(III) were utilized as single-source precursor compounds. Furthermore, the photoelectrochemical activities of the nanoparticles were studied.

2. RESULTS AND DISCUSSION

2.1. X-Ray Diffraction (XRD) Studies. Figure 1 presents the X-ray diffraction patterns of the nanoparticles. The diffraction pattern of Bi_2S_3 (Figure 1a) showed that all of the peaks corresponded to orthorhombic Bi_2S_3 with cell parameters a = 11.23 Å, b = 11.30 Å, and c = 3.98 Å; a space group of *Pbnm* (62); and 20 atoms per unit cell.[26] It matched very well with the powder diffraction file PDF No. 17-0320. The significantly enhanced (2 0 2) peak compared to the characteristic (1 3 0) diffraction peak of Bi_2S_3 revealed that there was a bias of orientations of the (2 0 2) crystallographic plane.[27] The sharp and well-defined peaks showed that the synthesized Bi_2S_3 nanoparticles were crystalline.[20] The XRD patterns of the Sb_2S_3 nanoparticles (Figure 1b) indicated the formation of the orthorhombic stibnite phase (JCPDS: 42-1393).[28] The structure has the lattice parameters of a = 11.23 Å, b = 11.31 Å, and c = 3.84 Å; and *Pnma* space group symmetry with the major peaks at 2θ = 28.0, 28.2, 31.1, and 31.3° corresponding to the (2 3 0), (2 1 1), (3 0 1), and (2 4 0) planes, respectively. In addition, the strong and sharp XRD peaks were indicative of the high crystallinity of the obtained Sb_2S_3. There were no other characteristic peaks ascribed to the Sb_2S_2O phase, which are sometimes observed in Sb_2S_3 nanoparticles prepared at elevated temperatures.[29] From XRD data, the crystallite diameters (D_c) of Bi_2S_3 and Sb_2S_3 nanoparticles were calculated to be 4.23 and 22.1 nm, respectively, using the Debye−Scherrer equation (eq 1)

$$D_c = K\lambda/\beta \cos\theta \quad (1)$$

where β is the breadth of the observed diffraction line at its half intensity maximum, K is the so-called shape factor and often takes a value of about 0.9, and λ is the wavelength of the X-ray source that was used in XRD.

2.2. Morphological Studies. The transmission electron microscopy (TEM) and high-resolution TEM (HRTEM) images of Bi_2S_3 and Sb_2S_3 are displayed in Figure 2. The morphologies of Bi_2S_3 nanoparticles (Figure 2a) were spherical and fairly well dispersed, which could be ascribed to the good passivation of the capping materials. The nanoparticles have morphologies similar to the bismuth sulfide reported in the literature.[30,31] Figure 2d shows that the Sb_2S_3 nanoparticles were also spherical and fairly dispersed but with a slight agglomeration. Biswal and Garje reported similar morphology for Sb_2S_3, which was prepared using antimony thiosemicarbazone as a single-source precursor and in ethylene glycol as a capping ligand.[32] The size distribution histograms of Bi_2S_3 and Sb_2S_3 are presented in Figure 2b,e, which showed mean crystallite sizes of 3.91 and 22.3 nm, respectively. The average sizes of the prepared nanoparticles were close to the observed

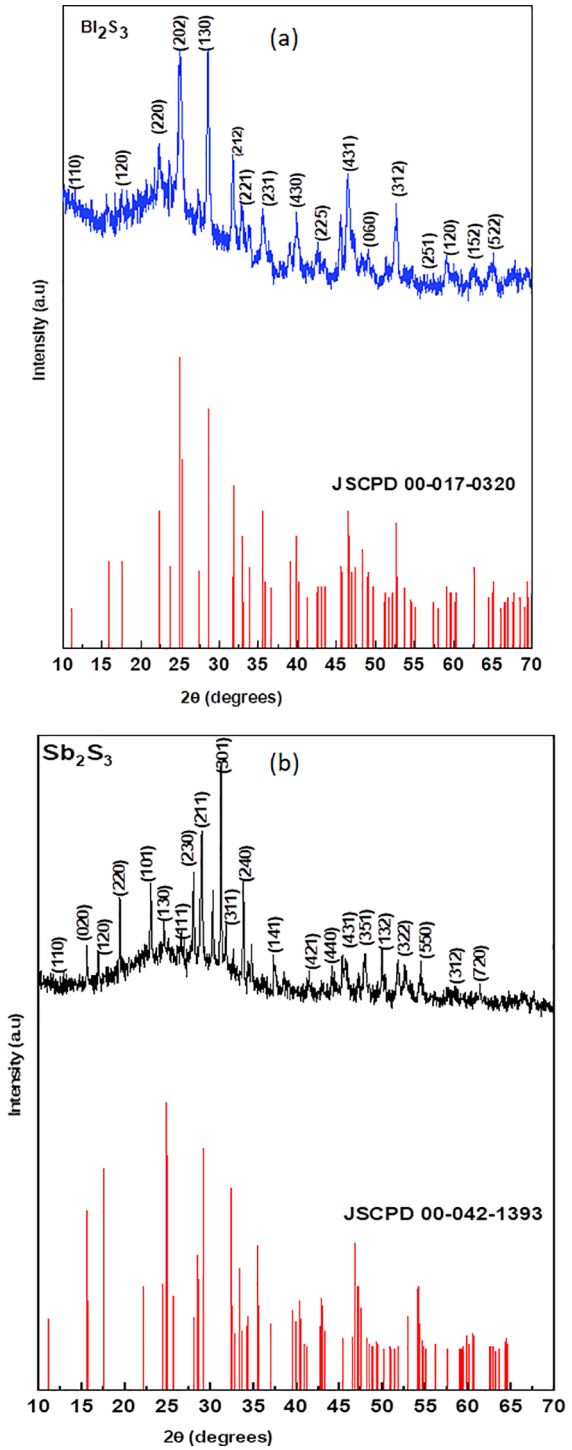

Figure 1. Powder XRD patterns of (a) Bi_2S_3 and (b) Sb_2S_3 nanoparticles obtained using *N*-methyl-*N*-ethanoldithiocarbamate complexes of Bi(III) and Sb(III) as single-source precursors.

https://doi.org/10.1021/acsomega.1c02249
ACS Omega 2021, 6, 18975−18987

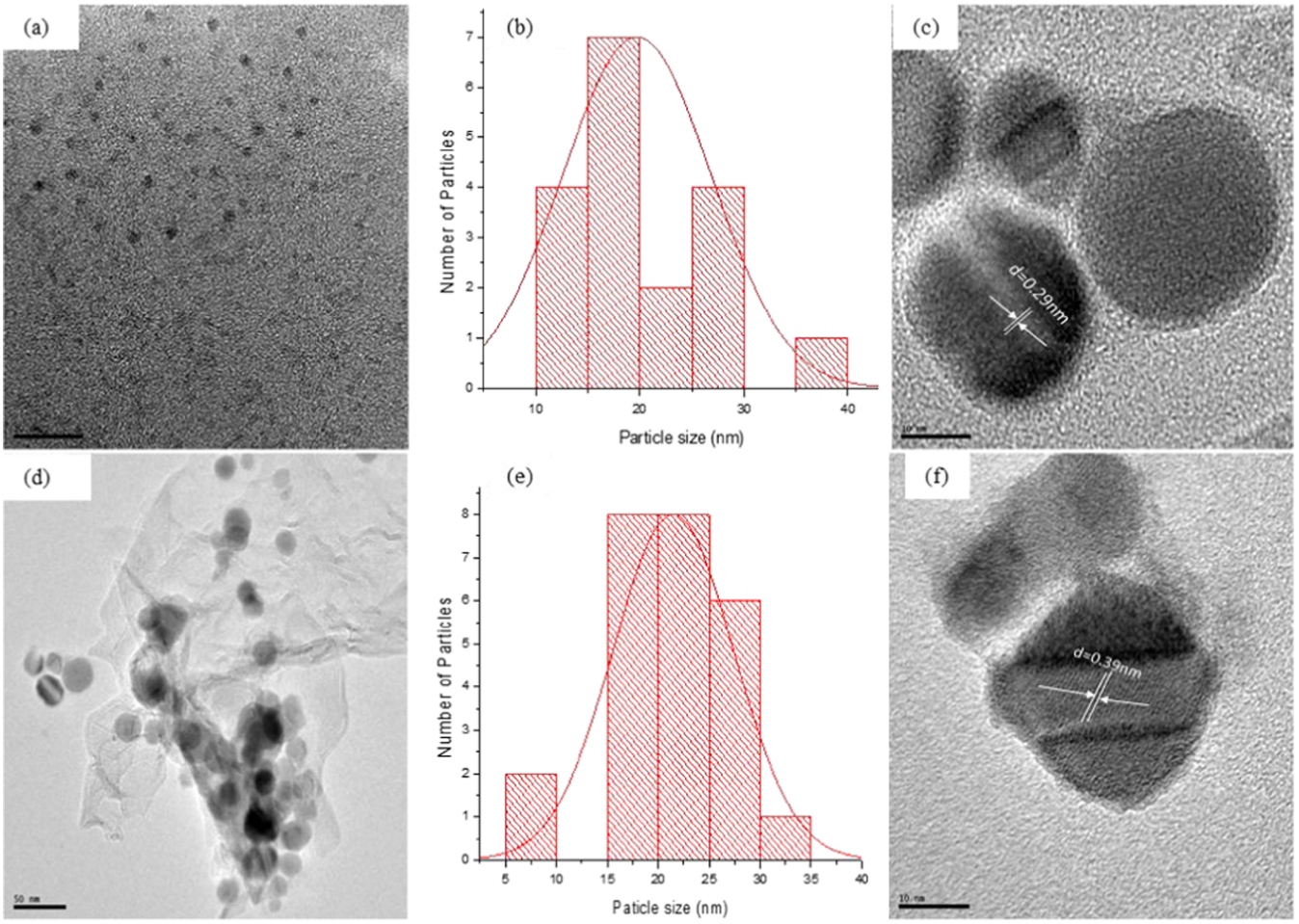

Figure 2. (a, d) TEM of Bi_2S_3 and Sb_2S_3; (b, e) size distribution histograms of Bi_2S_3 and Sb_2S_3; and (c, f) HRTEM micrographs of Bi_2S_3 and Sb_2S_3 nanoparticles.

crystallite size calculated from the XRD patterns. The HRTEM microgram shown in Figure 2c clearly displays an orthorhombic Bi_2S_3 crystal phase with the (1 2 0) plane,[33] whose lattice spacing distance of 0.35 nm was well identified. Figure 2f also shows the distinct lattice fringe, whose distance of 0.39 nm corresponded to the (2 0 1) plane of the Sb_2S_3 structure.[34]

The external morphology of the nanomaterials was investigated using scanning electron microscopy (SEM) analysis. Figure 3a presents the SEM micrograms of Bi_2S_3, which showed fairly aggregated spherical particles tending toward a grain-like morphology. The SEM image of Sb_2S_3 presented in Figure 3c reveals highly agglomerated particles, resulting in coagulated fragments. Elemental composition was determined by the energy-dispersive X-ray (EDX) measurement. The corresponding EDX spectra of Bi_2S_3 and Sb_2S_3 nanoparticles are presented in Figure 3b,d. The elemental composition of the nanoparticles established that the samples contained C, O, M (M = Bi, Sb), and S. The presence of carbon may be due to the carbon coating of the copper grid,[35] and the oxygen atom may be ascribed to long exposure to air during analysis.[36]

2.3. Optical Studies. The absorption studies of Bi_2S_3 and Sb_2S_3 nanoparticles have been achieved using UV−vis−NIR spectroscopy in the wavelength range of 200−1200 nm. The absorption spectrum of Bi_2S_3 presented in Figure 4a exhibited a broad band with a peak around 589 nm and a weaker absorption peak at 1173 nm. Figure 4c shows the absorption spectra of Sb_2S_3, which exhibited a broad absorption in the near-infrared region around 1120 nm. The optical band gap (E_g) energies were determined from the absorption coefficient (α) and photon energy ($E = h\nu$) using eq 2

$$(\alpha E)^2 = A(h\nu - E_g) \quad (2)$$

where A is a constant.[37] The band gap energy values (E_g) were obtained from the spectra by the extrapolation of the linear part of the curve giving 2.17 eV for Bi_2S_3, which was higher compared to the direct band gap of the bulk Bi_2S_3 (1.3 eV)[38] and this could be related to the morphology, size, and structure of the nanoparticles. Ranjbar and Taher[12] have reported similar shifting of the band gap energy of Bi_2S_3 to higher values. The obtained band gap value of 2.71 eV for Sb_2S_3 was found to be slightly higher compared to the band gap (1.78−2.5 eV) of the bulk material.[39] The blue shift observed in the band gap of Sb_2S_3 suggested the particle sizes, hence resulting in a stronger quantum confinement effect.[40,41]

The photoluminescence spectra of the nanoparticles measured at an excitation wavelength of 350 nm are shown in Figure 5. The spectrum of Bi_2S_3 nanoparticles (Figure 5a) showed a narrow emission peak at 358 nm and a small peak at 723 nm. The strong emission is ascribed to the recombination of trapped electron−hole pairs inside a sulfur vacancy in the valence band of the Bi_2S_3 nanoparticles,[42] while the lower-intensity peak may be ascribed to stoichiometric deviation in

https://doi.org/10.1021/acsomega.1c02249
ACS Omega 2021, 6, 18975−18987

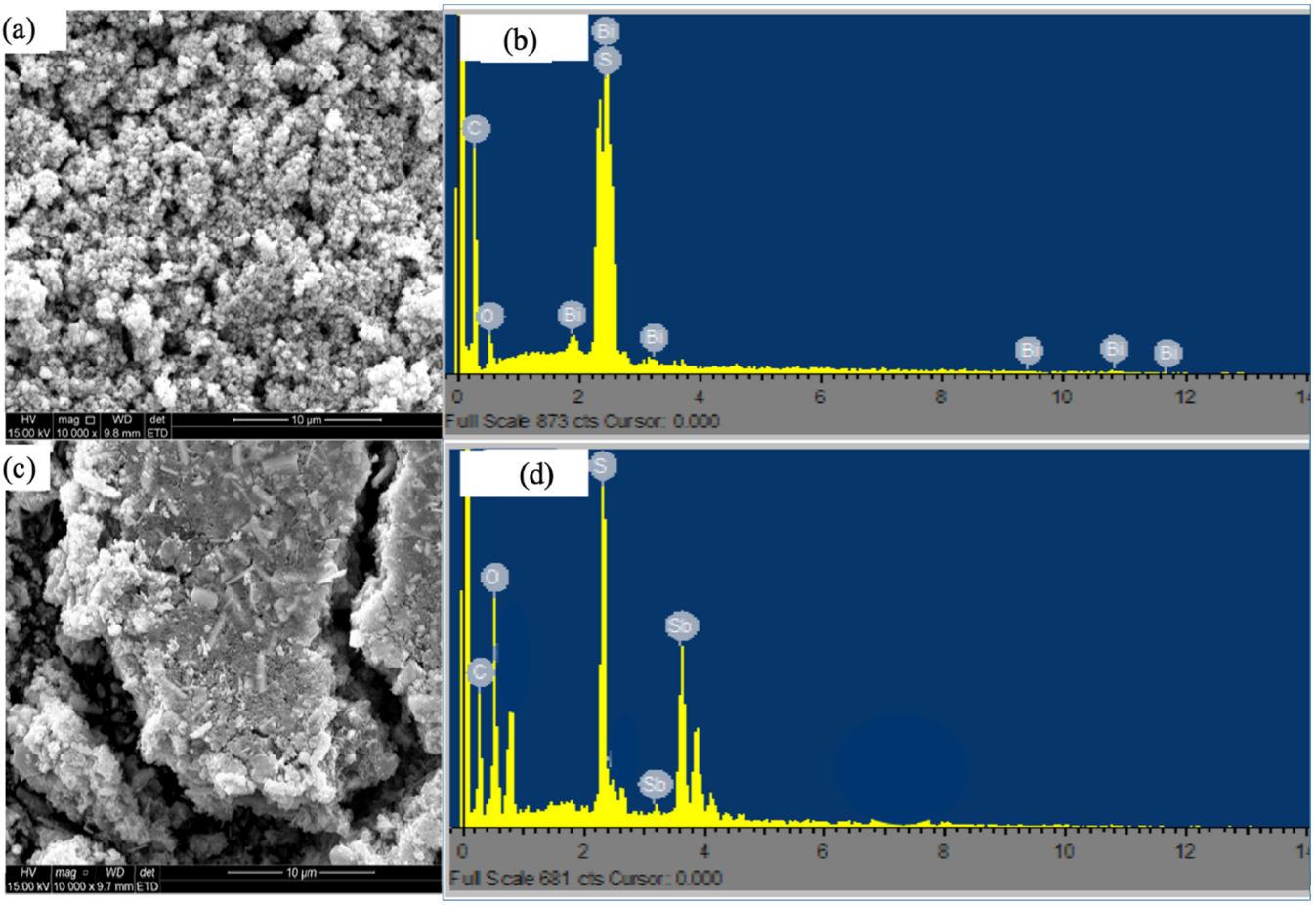

Figure 3. (a, c) SEM micrographs of Bi_2S_3 and Sb_2S_3; and (b, d) EDX of Bi_2S_3 and Sb_2S_3 nanoparticles, respectively.

the nanoparticles. Figure 5b presents the PL spectrum of Sb_2S_3 with a narrow emission at 573 nm. The emission may be attributed to a donor−acceptor transition between the antimony vacancy and the sulfur vacancy.[43]

2.4. Electrochemical Characterization. To determine the redox potential of the nanoparticles, cyclic voltammograms of the modified glassy carbon electrodes were measured in 5 mM $[Fe(CN)_6]^{4-}/[Fe(CN)_6]^{3-}$ redox couple at a potential window between −0.4 and +1.2 V, and the scan rate was 50 mV/s. Cyclic voltammetric evolution of glassy carbon-modified electrodes in 5 mM $[Fe(CN)_6]^{4-}/[Fe(CN)_6]^{3-}$ is shown in Figure 6. The voltammograms of bare Bi_2S_3 and Sb_2S_3 nanoparticles showed a pair of redox peaks with relatively comparable features. The anodic peaks were found around +0.35 V and cathodic peaks were present around +0.01 V. These peaks were ascribed to the electrochemical process associated with the $[Fe(CN)_6]^{4-}/[Fe(CN)_6]^{3-}$ reversible redox probe.[44] The behavior is characteristic of a Nernstian fast one-electron transfer reaction for a kinetically facile system.[45] The peak separation between the cathodic and anodic process for the redox reaction of the $[Fe(CN)]^{4-}/[Fe(CN)]^{3-}$ analyte was observed to be 410 and 352 mV for $GCEBi_2S3$ and $GCESb_2S_3$, respectively, which was far higher compared to the Nernstian type quasi-reversible case (56 mV). Furthermore, the ratio of I_{pa}/I_{pc} for $GCEBi_2S3$ and $GCESb_2S_3$ was closer to 1.0, which confirmed that the electrode reaction was reversible.[46] Furthermore, the modified electrodes did not show much change from GCEbare and, thus, the peak observed in the presence of Bi_2S_3 and Sb_2S_3 could be solely attributed to the $[Fe(CN)_6]^{4-}/[Fe(CN)_6]^{3-}$ analyte. The cyclic voltammogram of $GCESb_2S_3$ gave the lowest peak currents compared to the GCE. This could be attributed to the nature of the metal involved in Sb_2S_3 nanoparticles, which hinders the transfer of electrons at the GCE/$[Fe(CN)_6]^{3-/4-}$ interface.[47,48]

The effect of different scan rates (ν) on $GCEBi_2S_3$ and $GCESb_2S_3$ was investigated in a 5 mM $[Fe(CN)]^{4-}/[Fe(CN)]^{3-}$ solution. Voltammograms of $GCEBi_2S_3$ and $GCESb_2S_3$ showed a linear increase for both anodic and cathodic peaks when the scan rate increased from 10 to 100 mV/s, which indicated that the current is dependent on the scan rate (ν). This confirmed that there exists a charge exchange with the surface-confined and reversible immobilized redox transition on the modified electrode. Furthermore, the redox peak current increased linearly with the square root of the scan rates. From the linear regression of the data fitted in the Randles−Sevick, from which correlation coefficient (R^2) could be estimated, it was suggestive that the charge transfer was diffusion controlled.

All of the voltammograms showed typical faradic pseudo-capacitance behaviors fulfilled by the redox reaction, which demonstrates that the electrochemical activity and specific capacitance could be greatly affected by the change in the scan rate. Furthermore, the specific capacitance is calculated from cyclic voltammetry at a scan rate of 50 mV/s, using eq 3.[49]

$$C_s = I\Delta t/m\Delta V \quad (3)$$

https://doi.org/10.1021/acsomega.1c02249
ACS Omega 2021, 6, 18975−18987

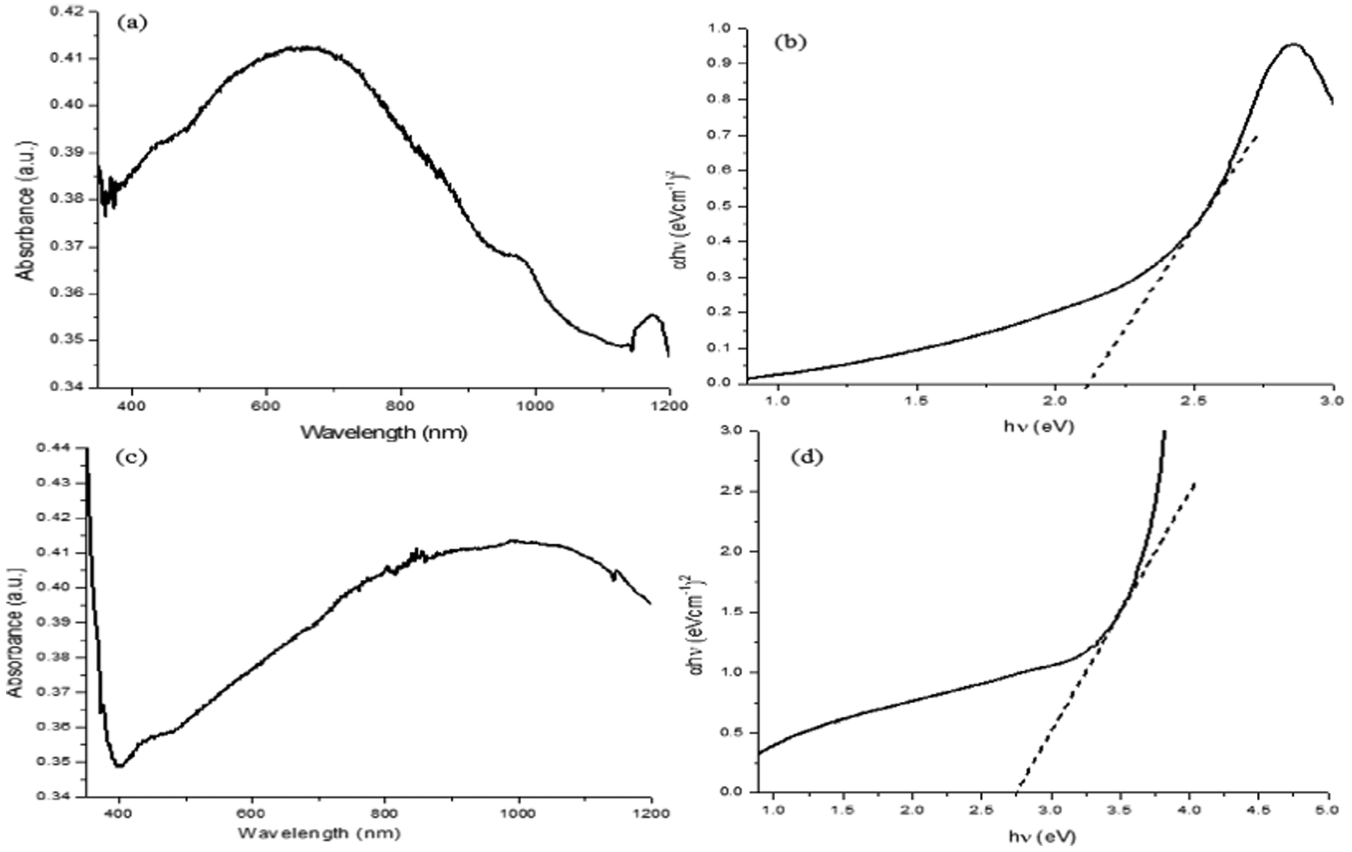

Figure 4. (a, c) UV−vis−NIR spectra of Bi_2S_3 and Sb_2S_3, and (c, d) the corresponding Tauc plot of Bi_2S_3 and Sb_2S_3, respectively.

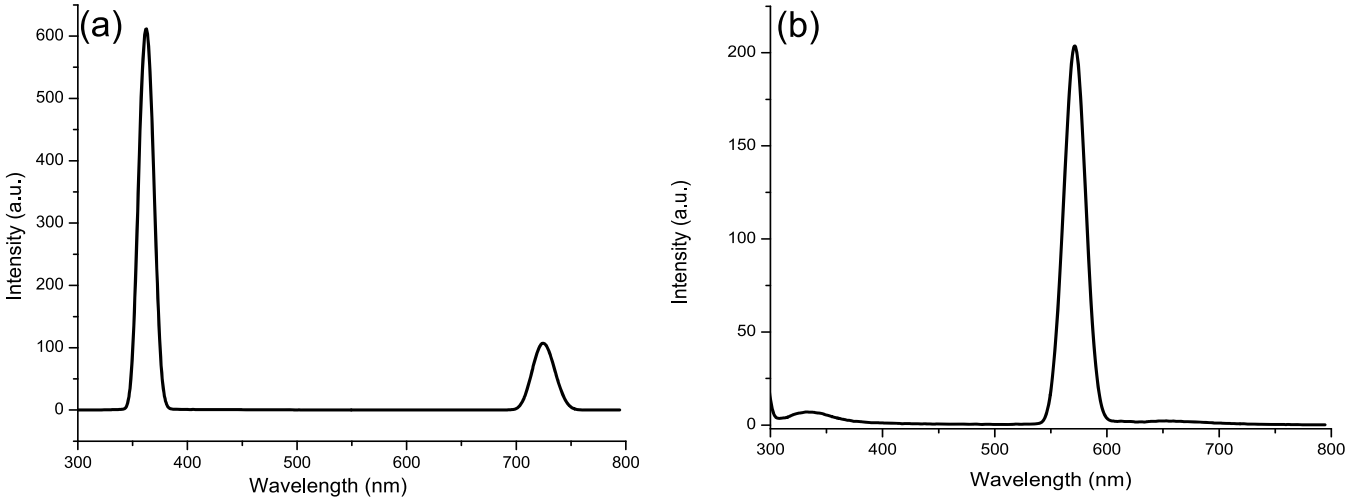

Figure 5. Photoluminescence spectra of (a) Bi_2S_3 and (b) Sb_2S_3 nanoparticles.

where C_s is the specific capacitance, ΔV $(V_f - V_i)$ is the potential window, m is the mass of the active material, and the term under the integration is the area under the curve. The estimated specific capacitance of GCEBi_2S_3 and GCESb_2S_3 was found to be 815 and 716 F/g, respectively, which are typical performances for electrochemical supercapacitors. This faradaic charge transfer is derived by a very fast sequence of reversible faradaic redox reactions on the surface of suitable electrodes. The Bi_2S_3 electrode exhibits higher specific capacitance compared to other electrodes, and this indicated that the $[Fe(CN)_6]^{4-}/[Fe(CN)_6]^{3-}$ solution provided high ionic conductivity and easier ion transport within the electrolyte, thereby leading to an effective build-up of redox reaction at the electrode surface. In addition, the specific capacitance calculated for the Bi_2S_3 modified electrode was found to be 816 F/g, which was significantly higher than bismuth sulfide nanoparticles reported by Devi et al.[20]

Figure 7 presents the square wave voltammetry (SWV) responses of the modified electrodes in the presence of 5 mM $[Fe(CN)]^{4-}/[Fe(CN)]^{3-}$, and scanned from −0.4 to +1.2 V vs the Ag/AgCl reference electrode. All square wave voltammograms at 50 mV/s for modified GCE showed well-defined peaks related to the anodic peak due to the $[Fe(CN)_6]^{4-}/[Fe(CN)_6]^{3-}$ oxidation reaction. The voltammogram of Bi_2S_3

https://doi.org/10.1021/acsomega.1c02249
ACS Omega 2021, 6, 18975−18987

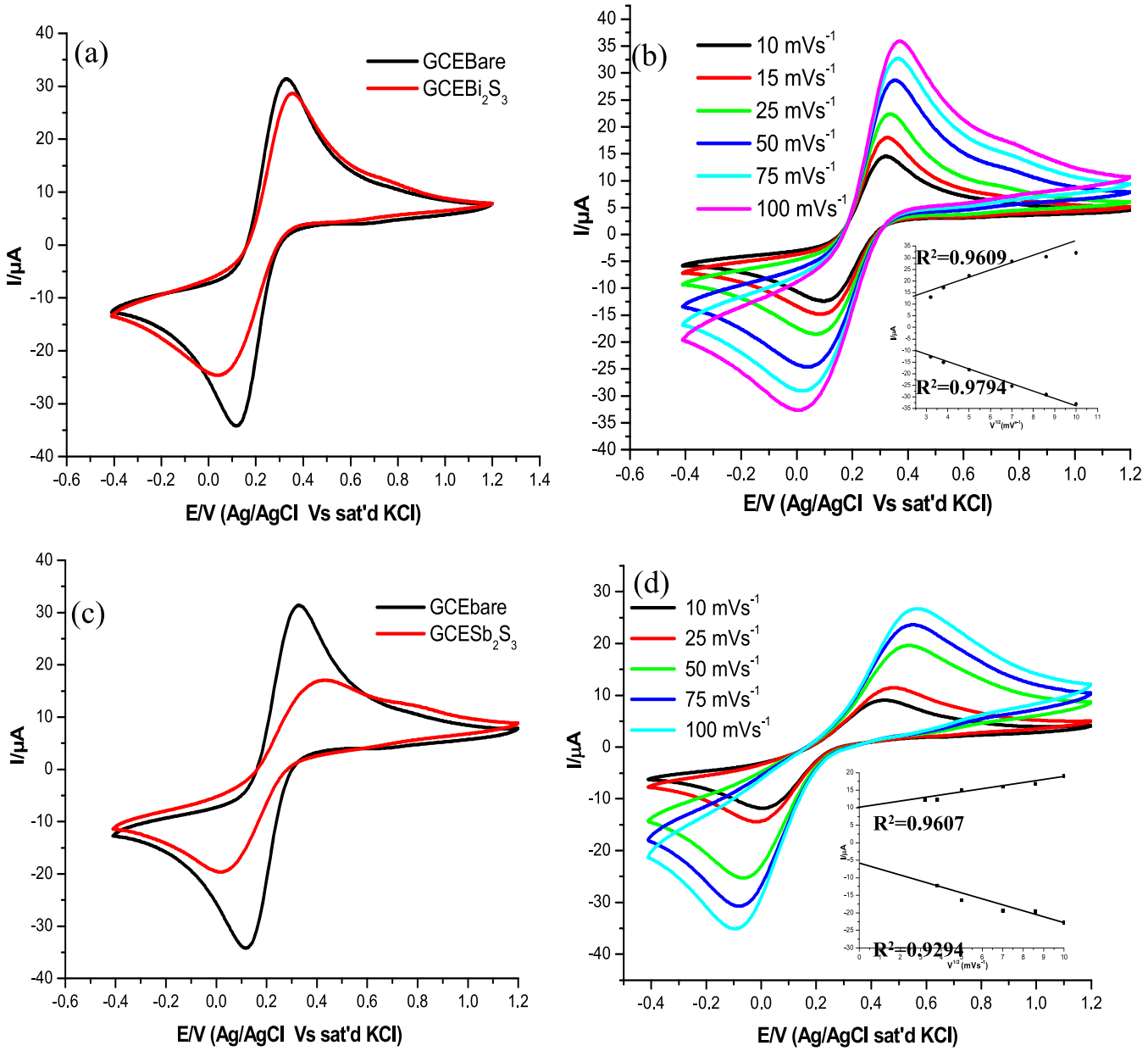

Figure 6. Cyclic voltammograms obtained for (a) GCEbare, $GCEBi_2S_3$ and (c) GCEbare, $GCESb_2S_3$; different scan rates (scan rate: 10−100 mV/s) with linear plots of I_{pa} vs $V^{1/2}$ and I_{pc} vs $V^{1/2}$ for (b) $GCEBi_2S_3$ and (b) $GCESb_2S_3$ in a 5 mM $[Fe(CN)]^{4-}/[Fe(CN)]^{3-}$ solution and (d) $GCESb_2S_3$ in a 5 mM $[Fe(CN)]^{4-}/[Fe(CN)]^{3-}$ solution.

was observed at a more positive anodic peak (+0.79 V) at a lower peak current. This marked decrease in current demonstrates the effect of Bi_2S_3 toward the oxidation of the $[Fe(CN)]^{4-}/[Fe(CN)]^{3-}$ analyte. The likelihood of a catalytic effect could not be ruled out even though the peak oxidation potential for $GCESb_2S_3$ occurred at a slightly lower potential than that of GCEbare. Square wave voltammogram of $GCESb_2S_3$ showed that a well-defined anodic peak was observed at +0.34 V at a lower oxidation peak current compared to GCEbare, which could be ascribed to the surface diffusion of Sb_2S_3 nanoparticles in the $[Fe(CN)]^{4-}/[Fe(CN)]^{3-}$ solution. Meanwhile, an obvious increase of the peak current is observed at the accumulation scan rate from 0 to 100 mV/s. As presented in the insert (Figure 7b,d), the corresponding calibration plots and correlation values showed a good linear relationship with the scan rate from 10 to 100 mV/s.

2.5. Electrochemical Impedance Spectroscopy (EIS). *2.5.1. Bode Plots for Nanoparticles.* Figure 8 shows the Bode plots fitted following the EIS results. The plot is representative of the characteristic frequency (f_{max}) of the charge transfer process occurring at the electrode/electrolyte interface and also that of the redox diffusion activity in the electrolyte.[50] The phase angles for GCEbare, $GCEBi_2S_3$, and $GCESb_2S_3$ were found to be constant at 44.1, 34.6, and 57.8°, respectively, which were less than 90°, suggesting that the electrodes experienced pseudo-capacitive behavior.[51] $GCESb_2S_3$ was observed at a lower characteristic frequency compared to $GCEBi_2S_3$ and indicated that $GCESb_2S_3$ was experienced at a slower charge recombination rate.[52,53] The redox diffusion of about 126 Hz was the slowest process among the charge

https://doi.org/10.1021/acsomega.1c02249
ACS Omega 2021, 6, 18975−18987

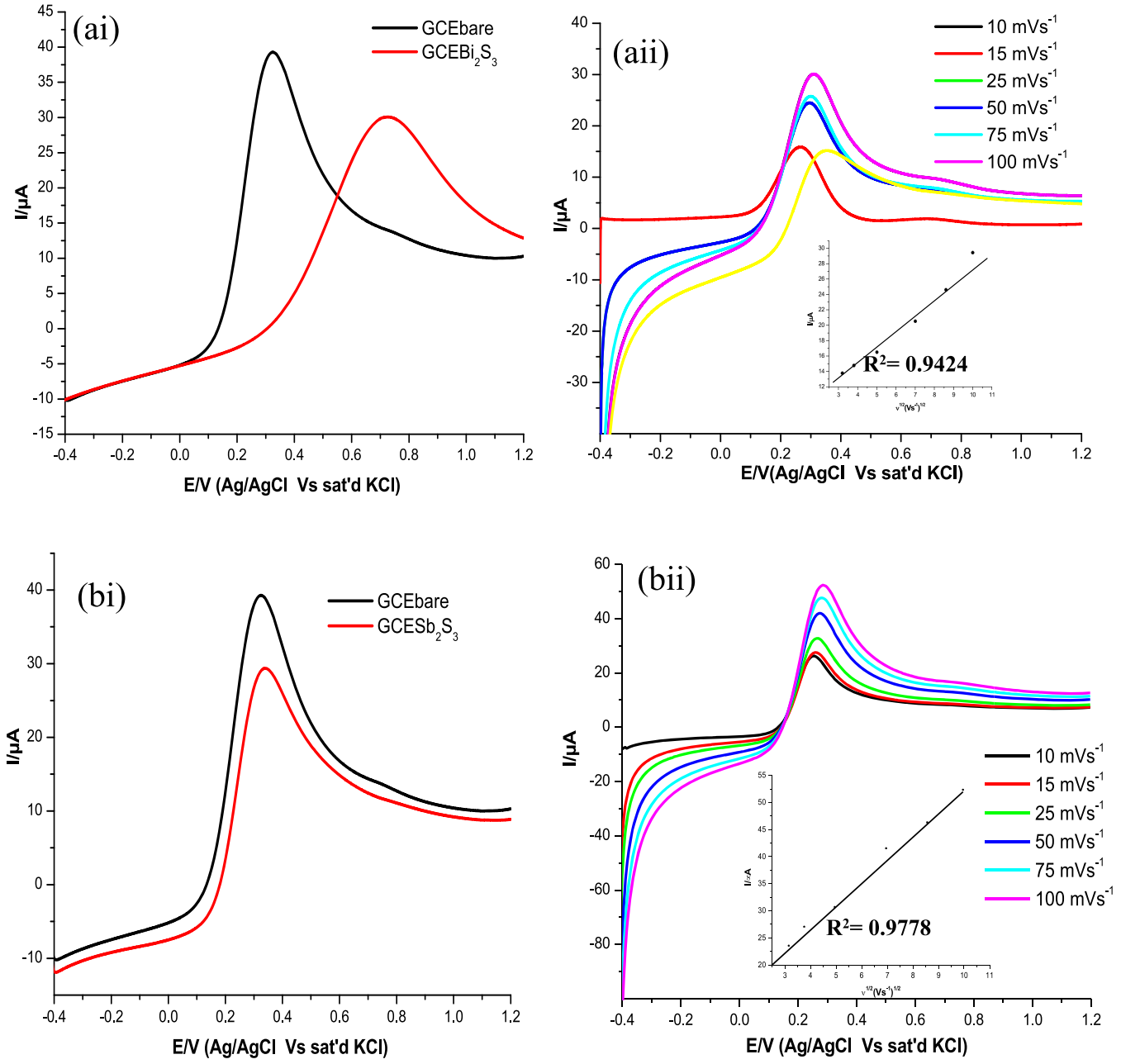

Figure 7. Square wave voltammograms obtained for (ai) GCEbare and GCEBi_2S_3, (bi) GCEbare and GCESb_2S_3, and with different scan rates (aii) GCEbare and GCEBi_2S_3, and (bii) GCEbare and GCESb_2S_3 (scan rate:10−100 mV/s) in 5 mM $[Fe(CN)_6]^{4-}/[Fe(CN)_6]^{3-}$.

transfer in all of the modified electrodes; hence, the determining process was associated with the electrocatalytic activity.[54,55] Although Sb_2S_3 was observed at a lower frequency, it was found to be considerably more than the frequency of the redox diffusion process in an electrolyte interface of solar cells. Hence, it completely meets the requirements for charge transfer in a photovoltaic cell.[56,57]

Bode plots of impedance spectra (plot of log|Z| vs log(frequency)) of the cells are presented in Figure 8. The plot demonstrates the frequency breakpoint related to the characteristic time constant $\tau = 1/\omega = R_sC_{dl}$ of the electrode−electrolyte circuit. The electrodes exhibited an f_0 (capacitor response frequency) at 119 Hz, which corresponded to constant time, τ, calculated to be 1.44 ms.[58] The electrodes possess a shorter electron lifetime compared to the other photoelectrodes.[59,60] In a typical photovoltaic cell, the electron lifetime is estimated to be in the range of 1−10 ms under open-circuit conditions and 1 sun illumination.[61] The impedance study clearly indicated that the Bi_2S_3 and Sb_2S_3 nanoparticles are semiconductor electrocatalysts.[62,63]

2.5.2. Nyquist Plots of the Nanoparticles. The plot presents the frequency response of the electrode−electrolyte system as a graph of the imaginary component (Z'') of the impedance vs the real component (Z'). The equivalent circuit, as shown in Figure 9b, of GCEbare comprised of the series resistance (R_s), the charge transport resistance (R_{ct}), and the constant phase element (CPE). The semicircle distance is related to R_{ct}, and the linear part, at lower frequencies, is associated with the diffusion process.[64−66] The impendence spectra show a semicircle in the region of high frequency and a straight line in the region of a low frequency, indicating that the modified electrodes have capacitive characteristics.[67,68] The

https://doi.org/10.1021/acsomega.1c02249
ACS Omega 2021, 6, 18975−18987

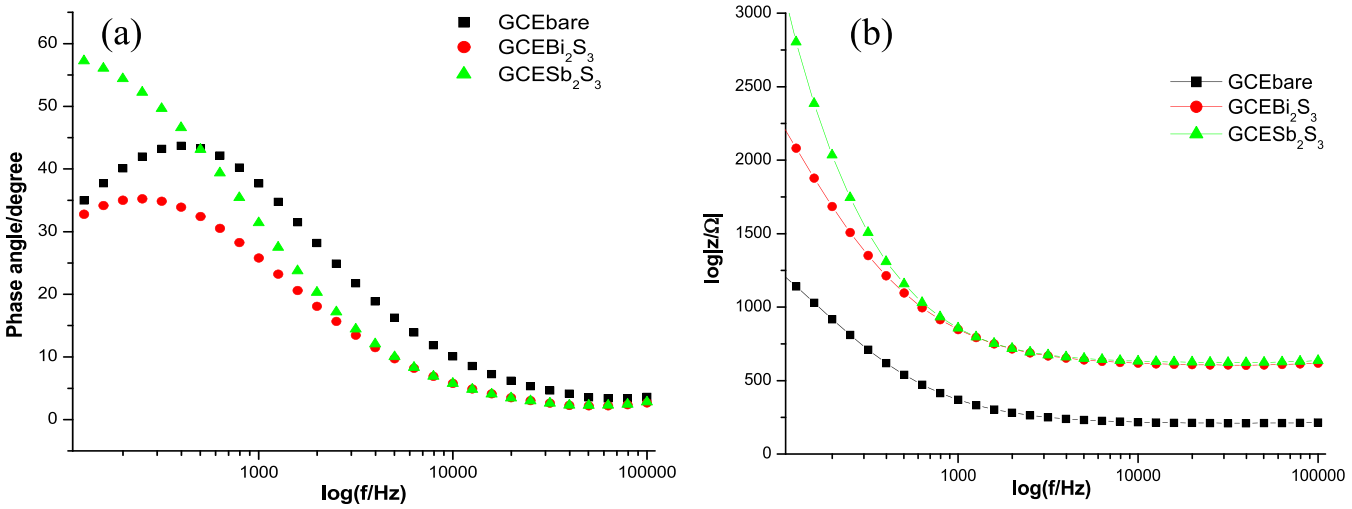

Figure 8. Electrochemical performance in 5 mM $[Fe(CN)_6]^{4-}/[Fe(CN)_6]^{3-}$ of GCEbare, $GCEBi_2S_3$, and $GCESb_2S_3$ (a) Bodes plots showing the plots of phase angle/degree vs log (f/Hz), and (b) the plot of log $|Z/\Omega|$ vs log (f/Hz).

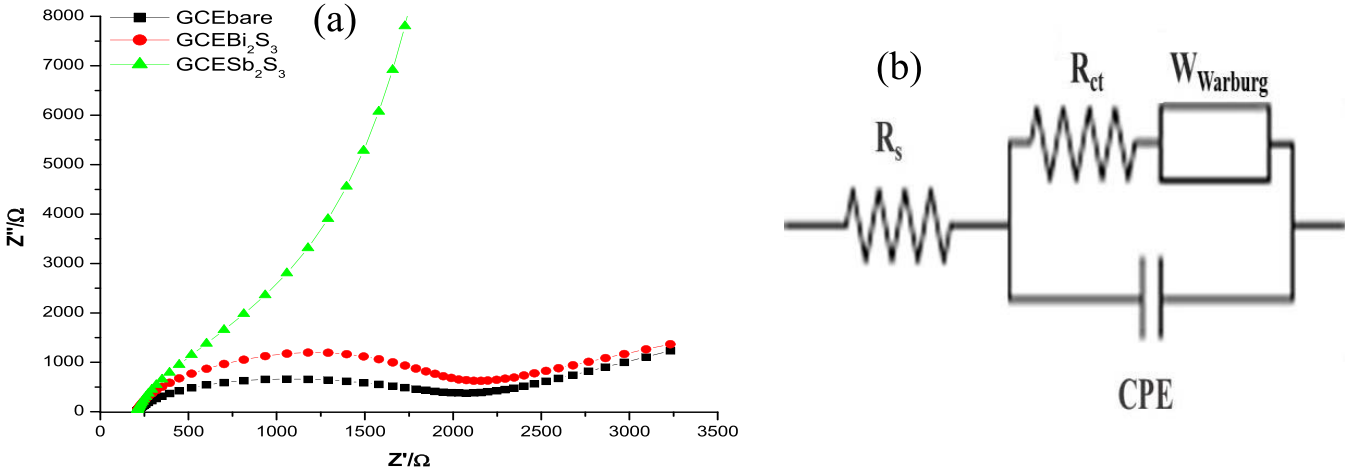

Figure 9. Electrochemical performance of GCEbare, $GCEBi_2S_3$, and $GCESb_2S_3$ in 5 mM $[Fe(CN)_6]^{4-}/[Fe(CN)_6]^{3-}$ (a) Nyquist plots and (b) circuit used in the fitting of EIS.

diameter of the semicircle is associated with the R_{ct}, assigned to the Faradaic process at the electrode/electrolyte interface.[69,70] The impedance spectra of $GCESb_2S_3$ were significantly different from GCEbare and $GCEBi_2S_3$. The Nyquist plots of $GCESb_2S_3$ are composed of a capacitance arc in the region of high frequency and a Warburg impedance line in the region of low frequency. This phenomenon was similar to literature reports by Karade et al. using antimony sulfide nanoparticles.[71] The impedance of the Sb_2S_3 electrode appears as a diagonal line with a slope of almost 45° in a complex plane plot. This indicated that Sb_2S_3-modified electrodes exhibited the property of resistance in the area of high frequency and also the property of capacitance in the area of low frequency, which is characteristic of the diffusion-controlled process.[44,72]

Based on the equivalent circuit fitted results, the R_s and R_{ct} values of modified electrons were observed to be lower compared to the value for the GCE. The decrease of the R_s values of $GCEBi_2S_3$ (120 Ω) and $GCESb_2S_3$ (147 Ω) and the R_{ct} values for $GCEBi_2S_3$ (78.1 Ω) and $GCESb_2S_3$ (138 Ω) indicated that the reduction of the $[Fe(CN)_6]^{4-}/[Fe(CN)_6]^{3-}$ electrolyte was higher in electrocatalytic activity in the cells. A similar observation was reported in the literature for different metal sulfide nanoparticles.[73] The larger the area of the semicircle, the slower the rate of electron transfer. The R_{ct} values from the equivalent circuit parameters of the nanoparticles were lower compared to the bare. However, the diameter of the semicircle was assigned to the electron transfer resistance (R_{ct}) of the redox process of the $[Fe(CN)]^{4-}/[Fe(CN)]^{3-}$ solution at the electrode interface, which was in good agreement with the cyclic measurements. The presence of the constant phase element (CPE) was associated with inhomogeneous nature at the electrode−electrolyte interface due to the diffusion of modified GCE surface into the $[Fe(CN)]^{4-}/[Fe(CN)]^{3-}$ solution.[6,71]

2.6. Current Density−Voltage Characterization. The electrospinning method was adopted for the preparation of Bi_2S_3 and Sb_2S_3 thin films.[53] Current density−voltage (J−V) characterization of a typical solar cell fabricated by electrospinning the solar cell device is shown in Figure 10a.

Figure 10b,c shows the current density−voltage (J−V) graph for Bi_2S_3 and Sb_2S_3 as the photovoltaic device. Poly(4-butylphenyldiphenyl-amine) (poly-TPD) was used as the transport layer and gold as the counter electrode. The solar cells were characterized under illumination at 100, 60, and 40 mW/cm^2

https://doi.org/10.1021/acsomega.1c02249
ACS Omega 2021, 6, 18975−18987

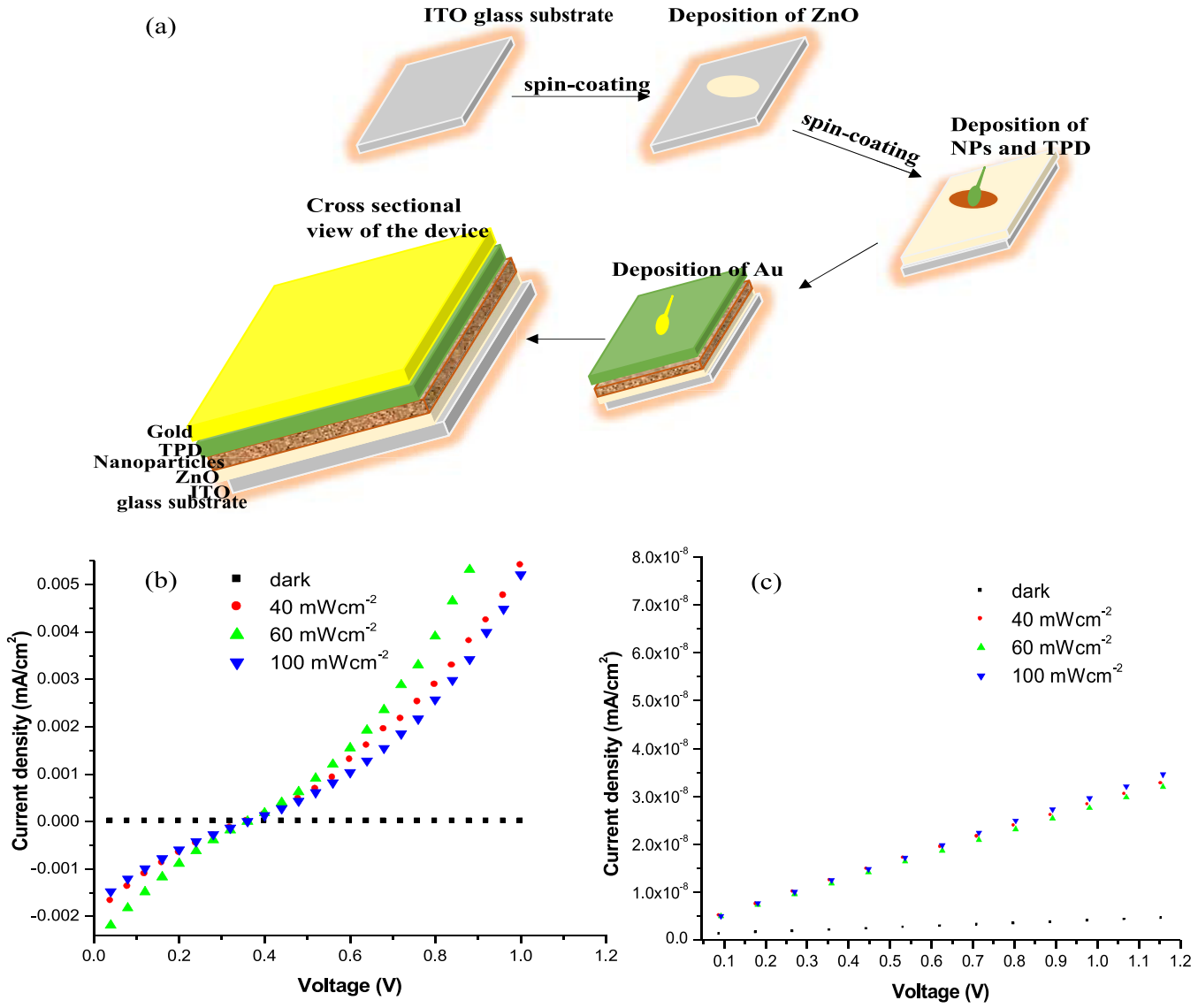

Figure 10. (a) Device fabrication by electrospinning and a cross-section of the device; and the $J-V$ plot for (b) Bi_2S_3 and (c) Sb_2S_3 thin films.

by a standard A.M. 1.5 solar simulator. Photovoltaic parameters of the cells like short-circuit current density (J_{sc}) and open-circuit voltage (V_{oc}) were obtained from the intercept on the current axis, and the fill factor (FF) value and efficiency (η) are summarized in Table 1. Figure 10c displays $J-V$ curves for Bi_2S_3, in which the value of J_{sc} was observed to increase with the increase in light illumination. The increase in the current after light illumination to 100 mW/cm^2 was ascribed to the generation of free electron−hole pairs in the conduction and valence bands due to high incident photons.[74] The device fabricated using Bi_2S_3 under 40 mW/cm^2 exhibited a power conversion efficiency (PCE) of 0.21%, with a V_{oc} of 0.94 V, a J_{sc} of 0.00152 mA/cm^2, and an FF of 43%. The performance (under 100 mW/cm^2) increased with a PCE of 0.39%, a V_{oc} of 0.96 V, a J_{sc} of 0.00228 mA/cm^2, and an FF of 44%. The results showed that an increase in the light intensity on the solar cell of the Bi_2S_3 thin film could increase the device performance. In addition, the voltammogram showed the nonlinear current density−voltage characteristics, indicating that Bi_2S_3 was experiencing the Schottky contact.[75] The efficiency of Bi_2S_3 was lower than in the similar work by Hussain and Rahman, but both devices have the Schottky character.[76] The $J-V$ curve for the Bi_2S_3 photovoltaic solar cell depicted a high solar efficiency at 100 mW/cm^2. This might be due to its near-infrared ability to absorb light at high intensity.[77,78] The Bi_2S_3 film might also have contributed to the higher photocurrent as a result of better connectivity with oxide species to produce recombination with holes, thereby resulting in a higher photocurrent and better efficiency.[41]

Table 1. Photovoltaic Parameters of the Bi_2S_3 Thin-Film Solar Cell Under Various Sun Intensities

structure	sun intensity (mW/m^2)	J_{sc} (mA/cm^2)	V_{oc} (V)	FF (%)	η (%)
FTO/ZnO/Bi_2S_3/TPD/Au	40	0.00152	0.94	43	0.21
	60	0.00162	0.93	33	0.15
	100	0.00228	0.96	44	0.39

The Sb_2-based thin film was observed to show no connection in the dark and under illumination. The $J-V$ curve shows a linear graph, which passed through the origin, both in the dark and under light irradiation, indicating the ohmic nature of the film. This might be due to the current

https://doi.org/10.1021/acsomega.1c02249
ACS Omega 2021, 6, 18975−18987

leakage caused by poor coverage. It may suffer from the large surface roughness, which leads to a larger amount of interfacial traps at the interface between Sb_2S_3 and ZnO. Poor connectivity between the two species may lead to an increase in the recombination rate between the electrons in Sb_2S_3/ZnO.[41] Castro et al. reported the synthesis of the Sb_2S_3 film, which was not characterized due to poor coverage.[79] No efficiency was recorded, hence, indicating that it might either be a window layer or a hole blocking layer.

3. EXPERIMENTAL SECTION

3.1. Materials. Ammonium solution, carbon disulfide, antimony(III) chloride, ethylene glycol, bismuth(III) chloride, methanol, *N*-methylethanol, potassium ferrocyanide, and dimethylformamide (DMF) were analytical reagents purchased from Sigma-Aldrich Co. and were used as received for the synthesis. Elemental analyses of C, H, N, and S were conducted using a Vario EL III elemental analyzer. The melting point was determined on an X4 melting point apparatus using capillary tubes. Fourier transform infrared (FTIR) spectra were measured on a Bruker α-P FTIR spectrophotometer at 4000−400 cm^{-1}. Nuclear magnetic resonance (NMR) (^1H and ^{13}C) analyses were performed using a 600 MHz Bruker-Avance III NMR spectrophotometer. TEM micrograms were obtained from a JEM-2100 JEOL electron microscope. X-ray diffraction (XRD) patterns were recorded on a Phillips X'Pert materials research diffractometer, which employs secondary graphite monochromated Cu Kα radiation (l = 1.54060 Å) at 40 kV/50 mA. Electrochemical experiments were conducted using an Autolab Potentiostat PGSTAT (Eco Chemie, Utrecht, The Netherlands) and GPES software version 4.9. The electrochemical impedance spectroscopy (EIS) was measured using Autolab NOVA software ranging from 100 kHz to 10 mHz with a 10 mV amplitude. The electroanalytical method was carried out in a three-electrode system, where platinum wire and saturated Ag/AgCl were applied as an auxiliary and reference electrode, respectively, and the GCE was used as a working electrode. Electrochemical impedance spectroscopy was performed with the working electrode biased at +0.20 V (vs reversible hydrogen electrode (RHE)) and superimposing a small sinusoidal voltage of 10 mV in the frequency ranging from 0.01 Hz to 100 kHz in the 5 mM $[Fe(CN)_6]^{4-}/[Fe(CN)_6]^{3-}$ solution. The Bode plot (the plot of phase angle vs log (frequency), and the plot of log |Z| vs log (frequency)), the Nyquist plots attained from the EIS examination, and the resultant circuit model were obtained from equivalent circuit fitting using Nova 2.1.3 software. The surface morphology of the film was analyzed using SEM. To characterize the solar cell, a Keithley 2400 source-meter that uses a voltage sweep at a rate of 0.01 V/s was used to record the current density−voltage characteristics. A solar simulator (Abet Technology Sun 2000), which was filtered to mimic air mass AM 1.5G conditions, was used to illuminate the solar cells. A reference silicon solar cell was used to calibrate the power density to 100 $mW{\cdot}cm^{-2}$, and a black mask was used to illuminate the surface to 0.07 cm^2.

3.2. Preparation of the Precursor. *N*-methyl-ethanol amine (0.01 mol, 0.8 mL) was introduced into a round bottom flask placed in an ice bath, then cold ammonium solution (3 mL) was added with continuous stirring. After 5 min, carbon disulfide (0.01 mol, 0.6 mL) was slowly added into the mixture. The solution was stirred for 3 h. Then, the respective (0.003 mol) metal salts (bismuth(III) nitrate, 1.05 g; antimony(III) nitrate, 0.684 g) in 10 mL of distilled water were used for the preparation. After the reaction, the precipitate was washed with water, followed by ethanol, and the solid product was recrystallized using chloroform.

Bismuth(III) tris(*N*-methyl-*N*-ethanoldithiocarbamate), $[BiL_3]$; yield: 1.23 g (61.9%); m.p.: 173−177 °C; selected FTIR, υ (cm^{-1}): 1483 (C−N), 1379 (C_2−N), 961 (C−S), 2921, 2869 (−CH), 3185 (OH), 460 (M−S); ^1H NMR ($CDCl_3$) δ ppm = 3.83 (t, 6H, $-C\underline{H}_2CH_2OH$), 4.49 (t, 6H, $-CH_2C\underline{H}_2OH$), 7.28 (s, 3H, $-CH_2CH_2O\underline{H}$), 3.61 (s, 9H, N−CH_3); ^{13}C NMR ($CDCl_3$) δ ppm = 60.5 ($-\underline{C}H_2CH_2OH$), 65.2 ($-CH_2\underline{C}H_2OH$), 50.4 (N−CH_3), 201.1 ($-CS_2$). $C_{12}H_{24}BiN_3O_3S_6$ (659.71): C, 21.80; H, 3.67; N, 6.37; S, 29.16. Found: C, 21.03; H, 3.82; N, 6.40; S, 29.24.

Antimony(III) tris(*N*-methyl-*N*-ethanoldithiocarbamate), $[SbL_3]$; yield: 1.59 g (81.2%); m.p.: 126−128 °C; selected FTIR, υ (cm^{-1}): 1448 (C−N), 1175 (C_2−N), 979 (C−S), 2929, 2868 (−CH), 3303 (OH), 447 (M−S); ^1H NMR ($CDCl_3$) δ = 3.96 (t, 6H, $-C\underline{H}_2CH_2OH$), 4.00 (t, 6H, $-CH_2C\underline{H}_2OH$), 7.19 (s, 3H, $-CH_2CH_2O\underline{H}$), 3.47 (s, 9H, N−CH_3); ^{13}C NMR ($CDCl_3$) δ ppm = 58.3 ($-\underline{C}H_2CH_2OH$), 60.5 ($-CH_2\underline{C}H_2OH$), 44.26 (N−CH_3), 205.0 ($-CS_2$). $C_{12}H_{24}N_3O_3S_6Sb$ (572.49): C, 25.18; H, 4.23; N, 7.34; S, 33.61. Found: C, 25.22; H, 4.26; N, 7.22; S, 33.03.

3.3. Synthesis of Nanoparticles (Bi_2S_3 and Sb_2S_3). The preparation of the Bi_2S_3 and Sb_2S_3 nanoparticles followed an already reported literature procedure.[25] Briefly, about 0.3 g of the respective complex $[BiL_3]$ or $[SbL_3]$ was dispersed in 30 mL ethylene glycol and sonicated for 10 min at 40 °C. The solution was then transferred into a poly(tetrafluoroethylene) (PTFE)-lined pressure-resistant microwave vessel and was left for the reaction to continue by cyclic microwave radiation at 800 W. After 5 min, the microwave heating was terminated and the solution was cooled to room temperature. The precipitate was washed with ethanol and air-dried.

3.4. Electrochemical Measurements. The electrochemical performances, comprising cyclic voltammetry (CV), square wave voltammetry (SWV), and electronic impedance spectroscopy (EIS), were carried out using a three-electrode electrochemical cell. In the cell, materials coated in a glassy carbon electrode were used as the modified electrode, Ag/AgCl (saturated with 4 M KCl) as the reference electrode, platinum wire as the counter electrode, and the 5 mM $[Fe(CN)]^{4-}/[Fe(CN)]^{3-}$ solution was used as an electrolyte. To modify the glassy carbon electrode, 5 mg of the corresponding Bi_2S_3 and Sb_2S_3 nanoparticles was dispersed into 1 mL of DMF and ultrasonicated for 30 min. Then, 5 μL of ink was dropped on a glassy carbon electrode and dried for 15 min in air.

3.5. Spin-Coating Deposition of Bi_2S_3 and Sb_2S_3 Thin Films. The solar cell devices were fabricated using two different substrates: bared glass and silicon slice. These two substrates (20 × 15 mm^2) were cleaned by ultrasonic treatment successively with water, acetone, and isopropanol and then subjected to UV−ozone treatment for 30 min. The Sb_2S_3 and Bi_2S_3 nanoparticles were dispersed in DMF and sonicated for 15 min for better dispersion. The solution was filtered through a 0.45 μm poly(vinylidene difluoride) (PVDF) syringe filter and was carefully spin-coated onto an ITO glass substrate coated with ZnO at 2000 rpm for 35 s using a Brewer Science spin coater (Model 200X), and then annealed at 90 °C for 15 min. Subsequently, two layers of poly(4-butyl-phenyl-

https://doi.org/10.1021/acsomega.1c02249
ACS Omega 2021, 6, 18975−18987

diphenyl-amine) (poly-TPD) used as the hole transport layers (1 wt % in chlorobenzene) were deposited through spin-coating at the same speed and then baked at 110 °C for 30 min. Finally, the top Au (100 nm thick) cathode was deposited as electrodes with a mask to fabricate photoconductive devices.

4. CONCLUSIONS

Bi_2S_3 and Sb_2S_3 nanoparticles have been successfully synthesized via a microwave-assisted route from *N*-methyl-*N*-ethanoldithiocarbamate complexes of Bi(III) and Sb(III) in ethylene glycol. Ethylene glycol used as a coordinating solvent afforded the formation of the orthorhombic phase of Bi_2S_3 and Sb_2S_3 with spherical morphologies. The nanoparticles exhibited direct band gap energies of 2.17 and 2.71 eV for Bi_2S_3 and Sb_2S_3, respectively, with optical spectra that extended from UV/visible to the near-IR region of the solar spectrum. Thus, these nanoparticles could have an interesting potential in the electrochemical and photovoltaic applications. The modified electrodes using the nanoparticles exhibited good electrochemical activity with an electron lifetime within the range of a typical photovoltaic cell under open-circuit conditions and one sun illumination. The nanoparticles were used to prepare thin films by the spin-coating method, and a model device photodetector was fabricated from the films using an electrospinning method. The device exhibited a linear response to the light intensity under illumination. The solar cells under illumination showed better performance and have the Schottky character, but Sb_2S_3 showed no change in the current, which led to poor photovoltaic performance. Hence, these nanoparticles have great potentials as light absorbers in photovoltaic cells.

AUTHOR INFORMATION

Corresponding Author

Damian C. Onwudiwe − *Material Science Innovation and Modelling (MaSIM) Research Focus Area, Faculty of Natural and Agricultural Science, North-West University, Mmabatho 2735, South Africa; Department of Chemistry, School of Physical and Chemical Sciences, Faculty of Natural and Agricultural Science, North-West University, Mmabatho 2735, South Africa;* orcid.org/0000-0002-2689-3981; Email: Damian.Onwudiwe@nwu.ac.za

Authors

Mathato P. Motaung − *Material Science Innovation and Modelling (MaSIM) Research Focus Area, Faculty of Natural and Agricultural Science, North-West University, Mmabatho 2735, South Africa; Department of Chemistry, School of Physical and Chemical Sciences, Faculty of Natural and Agricultural Science, North-West University, Mmabatho 2735, South Africa*

Wei Lei − *Joint International Research Laboratory of Information Display and Visualization, School of Electronic Science and Engineering, Southeast University, Nanjing 210096, China*

Complete contact information is available at: https://pubs.acs.org/10.1021/acsomega.1c02249

Notes

The authors declare no competing financial interest.

ACKNOWLEDGMENTS

M.P.M. acknowledges the award of a Ph.D. scholarship by the NRF/Sasol Inzalo Foundation, South Africa. The authors are grateful to Dr. Fuku of the Council for Scientific and Industrial Research (CSIR), Pretoria, for conducting electrochemical measurements.

REFERENCES

(1) Ranjbar, M.; Taher, M. A.; Rajaei, P. Preparation and characterization of bismuth sulfide (Bi_2S_3) nanostructures by ultrasonic method. *J. Ultrafine Grained Nanostruct. Mater.* **2014**, *47*, 15−19.

(2) Yeon, D. H.; Mohanty, C.; Lee, C. Y.; Lee, S. M.; Cho, Y. S. High-efficiency double absorber PbS/CdS heterojunction solar cells by enhanced charge collection using a ZnO nanorod array. *ACS Omega* **2017**, *2*, 4894−4899.

(3) Alemi, A.; Joo, S. W.; Hanifehpour, Y.; Khandar, A.; Morsali, A.; Min, B.-K. Hydrothermal Synthesis of Sb_2S_3 Nanorods Using Iodine via Redox Mechanism. *J. Nanomater.* **2011**, *2011*, No. 186528.

(4) Meng, X.; Wang, X.; Zhong, M.; Wu, F.; Fang, Y. Sb_2S_3 surface modification induced remarkable enhancement of TiO_2 core/shell nanowries solar cells. *J. Solid State Chem.* **2013**, *201*, 75−78.

(5) Hu, P.; Cao, Y.; Lu, B. Flowerlike assemblies of Bi_2S_3 nanorods by solvothermal route and their electrochemical hydrogen storage performance. *Mater. Lett.* **2013**, *106*, 297−300.

(6) Clark, R. M.; Kotsakidis, J. C.; Weber, B.; Berean, K. J.; Carey, B. J.; Field, M. R.; Khan, H.; Ou, J. Z.; Ahmed, T.; Harrison, C. J.; Cole, I. S.; Latham, K.; Kalantar-Zadeh, K.; Daeneke, T. Exfoliation of Quasi-stratified Bi_2S_3 crystals into micron-scale ultrathin corrugated nanosheets. *Chem. Mater.* **2016**, *28*, 8942−8950.

(7) Arumugam, J.; Raj, A. D.; Irudayaraj, A. A.; Thambidurai, M. Solvothermal synthesis of Bi_2S_3 nanoparticles and nanorods towards solar cell application. *Mater. Lett.* **2018**, *220*, 28−31.

(8) Arumugam, J.; Raj, A. D.; Irudayaraj, A. A. Reaction time dependent investigation on the properties of the Bi_2S_3 nanoparticles: photocatalytic application. *Mater. Today: Proc.* **2018**, *5*, 16094−16099.

(9) Huerta-Flores, A. M.; García-Gómez, N. A.; de la Parra, S. M.; Sánchez, E. M. Comparative study of Sb_2S_3, Bi_2S_3 and In_2S_3 thin film deposition on TiO_2 by successive ionic layer adsorption and reaction (SILAR) method. *Mater. Sci. Semicond. Process.* **2015**, *37*, 235−240.

(10) Chauhan, R.; Chaturvedi, J.; Trivedi, M.; Singh, J.; Molloy, K. C.; Kociok-Köhn, G.; Amalnerkar, D. P.; Kumar, A. New single-source precursor for bismuth sulfide and its use as low-cost counter electrode material for dye-sensitized solar cells. *Inorg. Chim. Acta* **2015**, *430*, 168−175.

(11) Moon, D. G.; Rehan, S.; Ahn, S.; Soo, Y.; Yeon, D. H.; Lee, S. M.; Park, S. J. A review on binary metal sulfide heterojunction solar cells. *Sol. Energy Mater. Sol. Cells* **2019**, *200*, No. 109963.

(12) Ranjbar, M.; Taher, M. A. Synthesis and characterization of bismuth sulfide nanostructures by new precursor with ultrasonic method. *Synth. React. Inorg., Met.−Org., Nano-Met. Chem.* **2016**, *46*, 1801−1804.

(13) Lu, H.; Guo, Q.; Zan, F.; Xia, H. Bi_2S_3 nanoparticles anchored on graphene nanosheets with superior electrochemical performance for supercapacitors. *Mater. Res. Bull.* **2017**, *96*, 471−477.

(14) Zhang, J.; Wang, H.; Yuan, X.; Zeng, G.; et al. Tailored indium sulfide-based materials for solar-energy conversion and utilization. *J. Photochem. Photobiol., C* **2019**, *38*, 1−26.

(15) Chao, J.; Xing, S.; Zhao, Y.; Gao, S.; Song, Q.; Guo, L.; Wang, D.; Zhang, T. Bismuth sulfide nano flakes and nanorods as high performance photodetectors and photoelectrochemical cells. *Solid State Sci.* **2016**, *61*, 51−57.

(16) Chao, J.; Xing, S.; Zhang, J.; Qin, C.; Duan, D.; Wu, X.; Shen, Q. Synthesis of Sb_2S_3 nanowall arrays for high performance visible light photodetectors. *Mater. Res. Bull.* **2014**, *57*, 300−305.

(17) Woods-Robinson, R.; Han, Y.; Zhang, H.; Ablekim, T.; Khan, I.; Persson, K.; Zakutayev, A. Wide band gap chalcogenide semiconductors. *Chem. Rev.* **2020**, *120*, 4007−4055.
(18) Zdanowicz, T.; Rodziewicz, T.; Zabkowska-Waclawek, M. Theoretical analysis of the optimum energy band gap of semiconductors for fabrication of solar cells for applications in higher latitudes locations. *Sol. Energy Mater. Sol. Cells* **2005**, *87*, 757−769.
(19) Zumeta-Dubé, I.; Ruiz-Ruiz, V.-F.; Díaz, D.; Rodil-Posadas, S.; Zeinert, A. TiO_2 sensitization with Bi_2S_3 quantum dots: The inconvenience of sodium ions in the deposition procedure. *J. Phys. Chem. C* **2014**, *118*, 11495−11504.
(20) Devi, N.; Ghosh, S.; Mallick, K. Supercapacitive performance of highly dispersed bismuth sulfide nanoparticles in organic matrix: the role of sulphur source. *Inorg. Chem. Commun.* **2019**, *103*, 93−99.
(21) Ranjitha, S.; Rajarajan, G.; Marimuthu, J.; Natarajan, S.; Vadivel, S. Structural and optical properties of bismuth sulfide nanoparticles. *Int. J. Sci. Res.* **2014**, *2014*, 9−12.
(22) Garza, D.; Palma, M. I. M.; Avellaneda, D.; Castillo, G. A.; Roy, T. K. D.; Krishnan, B.; Shaji, S.; et al. Nanoparticles of antimony sulfide by pulsed laser ablation in liquid media. *J. Mater. Sci.* **2013**, *48*, 6445−6453.
(23) Zhu, Y. J.; Chen, F. Microwave-assisted preparation of inorganic nanostructures in liquid phase. *Chem. Rev.* **2014**, *114*, 6462−6555.
(24) Hwang, S. M.; Kim, J.; Kim, Y.; Kim, Y. Na-ion storage performance of amorphous Sb_2S_3 nanoparticles: anode for Na-ion batteries and seawater flow batteries. *J. Mater. Chem. A* **2016**, *4*, 17946−17951.
(25) Onwudiwe, D. C. Microwave-assisted synthesis of PbS nanostructures. *Heliyon* **2019**, *5*, No. e01413.
(26) Larson, P.; Greanya, V. A.; Tonjes, W. C.; Liu, R.; Mahanti, S. D.; Olson, C. G. electronic structure of Bi_2 X_3 (X = S, Se, T) compounds: Comparison of Theoretical calculations with photoemission studies. *Phys. Rev. B* **2002**, *65*, No. 085108.
(27) Salavati-Niasari, M.; Ghanbari, D.; Davar, F. Synthesis of different morphologies of bismuth sulfide nanostructures via hydrothermal process in the presence of thioglycolic acid. *J. Alloys Compd.* **2009**, *488*, 442−447.
(28) Sheikhiabadi, P. G.; Salavati-Niasari, M.; Davar, F. Hydrothermal synthesis and optical properties of antimony sulfide micro and nano-size with different morphologies. *Mater. Lett.* **2012**, *71*, 168−171.
(29) Xiang, W. D.; Ji, G. Y.; Jing, W.; Yang, Y. X.; Liu, X. N. Study on the synthesis of water-soluble Sb_2S_3. *Glass Phys. Chem.* **2012**, *38*, 245−253.
(30) Devi, N.; Ghosh, S.; Mallick, K. Supercapacitive performance of highly dispersed bismuth sulfide nanoparticles in organic matrix: the role of sulphur source. *Inorg. Chem. Commun.* **2019**, *103*, 93−99.
(31) Perla, V. K.; Ghosh, S. K.; Pal, T.; Mallick, K. Organic molecule stabilized bismuth sulfide nanoparticles: a potential system for bistable resistive memory application. *Physica E* **2020**, *116*, No. 113787.
(32) Biswal, J. B.; Garje, S. S. Preparation of antimony sulfide nanostructures from single-source antimony thiosemicarbazone precursors. *Synth. React. Inorg., Met.-Org., Nano-Met. Chem.* **2013**, *43*, 461−465.
(33) Mahapatra, A. D.; Basak, D. Enhanced Ultraviolet Photosensing properties in Bi_2S_3 nanoparticles decorated ZnO nanorods' heterostructure. *J. Alloys Compd.* **2019**, *797*, 766−774.
(34) Dutková, E.; Takacs, L.; Sayagués, M. J.; Baláž, P.; Kováč, J.; Šatka, A. Mechanochemical synthesis of Sb_2S_3 and Bi_2S_3 nanoparticles. *Chem. Eng. Sci.* **2013**, *85*, 25−29.
(35) Revaprasadu, N.; Malik, M. A.; O'Brien, P. Synthesis of TOPO-capped nanocrystals of copper sulphide from a single-source precursor, $[Cu(S_2CNMe(NHex))_2]$. *S. Afr. J. Chem.* **2004**, *57*, 40−43.
(36) Mourdikoudis, S.; Liz-Marzán, L. M. Oleylamine in nanoparticle synthesis. *Chem. Mater.* **2013**, *25*, 1465−1476.
(37) Lajnef, M.; Ezzaouia, H. Structural and optical studies of In_2S_3 thin films prepared by sulferization of indium thin films. *Open Appl. Phys. J.* **2009**, *2*, 23−26.
(38) Han, Q.; Chen, J.; Yang, X.; Lu, D.; Wang, X. Preparation of uniform Bi_2S_3 nanorods using xanthate complexes of bismuth(III). *J. Phys. Chem. C* **2007**, *111*, 14072−14077.
(39) Cheng, B.; Samulski, E. T. One-step, ambient-temperature synthesis of antimony sulfide (Sb_2S_3) micron-size polycrystals with a spherical morphology. *Mater. Res. Bull.* **2003**, *38*, 297−301.
(40) Verma, S.; Agrawal, V.; Jain, K.; Pasricha, R.; Chand, S. Green synthesis of nanocrystalline Cu_2ZnSnS_4 powder using hydrothermal route. *J. Nanopart.* **2013**, *2013*, No. 685836.
(41) Buatong, N.; Tang, I.; Pon-On, W. Fabrication of solar cells made with $CuInTe_{2x}Se_x$ quantum dots sensitized hierarchical TiO_2 sphere having a CuS counter electrode: dependence on the Te/Se ratio. *Mater. Lett.* **2017**, *199*, 41−45.
(42) Murugadoss, G.; Jayavel, R.; Kumar, M. R. Structural, optical and thermal properties of CdS/Bi_2S_3 nanocomposites. *Indian J. Phys.* **2016**, *90*, 173−178.
(43) Suriyanarayanan, N.; Mahendran, C. Effect of temperature on structural, optical and photoluminescence properties of antimony (Sb) doped polycrystalline $CuInS_2$ thin films prepared by spray pyrolysis. *Mater. Sci. Eng. B* **2011**, *176*, 417−424.
(44) Wan, Q.; Song, H.; Shu, H.; Wang, Z.; Zou, J.; Yang, N. In situ synthesized gold nanoparticles for direct electrochemistry of horseradish peroxidase. *Colloids Surf., B* **2013**, *104*, 181−185.
(45) Bridge, M. H.; Williams, E.; Lyons, M. E. G.; Tipton, K. F.; Linert, W. Electrochemical investigation into the redox activity of Fe(II)/Fe(III) in the presence of nicotine and possible relations to neurodegenerative diseases. *Biochim. Biophys. Acta* **2004**, *1690*, 77−84.
(46) Wang, W.; Fan, X.; Liu, J.; Yan, C.; Zeng, C. Temperature-related reaction kinetics of the vanadium (IV)/(V) redox couple in acidic solutions. *RSC Adv.* **2014**, *4*, 32405−32411.
(47) Valiulienė, G.; Žielienė, A.; Šimkūnaitė, B.; Naruškevičius, L.; Tamašiūnaitė, L. T.; Pakštas, V.; Selskis, A. Electrochemical modification of Bi_2S_3 coatings in a nickel plating electrolyte. *J. Solid State Electrochem.* **2010**, *14*, 203−212.
(48) Guo, T.; Song, Y.; Sun, Z.; Wu, Y.; Xia, Y.; Li, Y.; Sun, J.; Jiang, K.; Dou, S.; Sun, J. bio-templated formation of defect-abundant VS_2 as a bifunctional material toward high-performance hydrogen evolution reactions and lithium-sulfur batteries. *J. Energy Chem.* **2020**, *42*, 34−42.
(49) Sahoo, R. K.; Singh, S.; Yun, J. M.; Kwon, S. H.; Kim, K. H. Sb_2S_3 nanoparticles anchored or encapsulated by the sulfur-doped carbon sheet for high-performance supercapacitors. *ACS Appl. Mater. Interfaces* **2019**, *11*, 33966−33977.
(50) Bisquert, J.; Mora-Sero, I.; Fabregat-Santiago, F. Impedance spectroscopy: a general introduction and application to dye-sensitized solar cells. *ChemElectroChem* **2014**, *1*, 289−296.
(51) Krishnamoorthy, K.; Kumar, G.; Jae, S. Hydrothermal synthesis, characterization and electrochemical properties of cobalt sulfide nanoparticles. *Mater. Sci. Semicond. Process.* **2015**, *40*, 781−786.
(52) Ahn, H. J.; Thogiti, S.; Cho, J. M.; Jang, B. Y.; Kim, J. H. Comparison of triphenylamine based single and double branched organic dyes in dye-sensitized solar cells. *Electron. Mater. Lett.* **2015**, *11*, 822−827.
(53) Habib, M.; Saha, S.; Sarkar, R.; Pramanik, A.; Sarkar, P.; Pal, S. Computational design of some TTF-substituted acene-based dyes for solar cell application using hollow ZnO quantum dot as acceptor. *Comput. Theor. Chem.* **2018**, *1136−1137*, 10−17.
(54) Peng, H.; Liang, R.; Zhang, L.; Qiu, J. Synthesis of magnetic core−shell $Fe_3O_4@ZrO_2$ nanoparticles and their application to the highly effective immobilization of myoglobin for direct electrochemistry. *Electrochim. Acta* **2011**, *56*, 4231−4236.
(55) Ghoreishi, S. M.; Behpour, M.; Khayatkashani, M. Green synthesis of silver and gold nanoparticles using rosa damascena and its primary application in electrochemistry. *Physica E* **2011**, *44*, 97−104.
(56) Xu, S.; Cheng, N.; Yin, H.; Cao, D.; Mi, B. Electrospray preparation of $CuInS_2$ films as efficient counter electrode for dye-sensitized solar cells. *Chem. Eng. J.* **2020**, *397*, No. 125463.

https://doi.org/10.1021/acsomega.1c02249
ACS Omega 2021, 6, 18975−18987

(57) Siemons, N.; Serafini, A. Multiple exciton generation in nanostructures for advanced photovoltaic cells. *J. Nanotechnol.* **2018**, *2018*, No. 7285483.
(58) Sarker, S.; Ahammad, A. J. S.; Seo, H. W.; Kim, D. M. Electrochemical impedance spectra of dye-sensitized solar cells: fundamentals and spreadsheet calculation. *Int. J. Photoenergy* **2014**, *2014*, No. 851705.
(59) Dutta, A.; Bhaumik, A. Nanopores in semiconducting oxides: optoelectronic and solar cell applications. *J. Nanosci. Nanotechnol.* **2013**, *13*, 2471−2482.
(60) Wang, H.; Gonzalez-Pedro, V.; Kubo, T.; Fabregat-Santiago, F.; Bisquert, J.; Sanehira, Y.; Nakazaki, J.; Segawa, H. Enhanced carrier transport distance in colloidal pbs quantum-dot-based solar cells using ZnO nanowires. *J. Phys. Chem. C* **2015**, *119*, 27265−27274.
(61) Boschloo, G. Improving the performance of dye-sensitized solar cells. *Front. Chem.* **2019**, *7*, No. 77.
(62) Elemike, E. E.; Fayemi, O. E.; Ekennia, A. C.; Onwudiwe, D. C.; Ebenso, E. E. Silver nanoparticles mediated by Costus afer leaf electrochemical properties. *Molecules* **2017**, *22*, No. 701.
(63) Balis, N.; Dracopoulos, V.; Bourikas, K.; Lianos, P. Quantum dot sensitized solar cells based on an optimized combination of ZnS, CdS and CdSe with CoS and CuC counter electrodes. *Electrochim. Acta* **2013**, *91*, 246−252.
(64) Zhao, X.; Quan, Y.; Pan, H.; Li, Q.; Shen, Y.; Huang, Z.; Wang, M. Novel donor-acceptor-donor structured small molecular hole transporting materials for planar perovskite solar cells. *J. Energy Chem.* **2019**, *32*, 85−92.
(65) Sun, J. K.; Jiang, Y.; Zhong, X.; Hu, J. S.; Wan, L. J. Three-dimensional nanostructured electrodes for efficient quantum-dot-sensitized solar cells. *Nano Energy* **2017**, *32*, 130−156.
(66) Cárdenas Riojas, A. A.; Wong, A.; Planes, G. A.; Sotomayor, M. D. P. T.; et al. Development of a new electrochemical sensor based on silver sulfide nanoparticles and hierarchical porous carbon modified carbon paste electrode for determination of cyanide in river water samples. *Sens. Actuators, B* **2019**, *287*, 544−550.
(67) Liang, K.; Wang, C.; Xu, X.; Leng, J.; Ma, H. Capacitive and photocatalytic performance of Bi_2S_3 nanostructures synthesized by solvothermal method. *Phys. Lett. A* **2017**, *381*, 652−657.
(68) Jia, Z.; Cui, Z.; Tan, Y.; Liu, Z.; Guo, X. Bimetal-organic frameworks derived ternary metal sulphide nanoparticles embedded in porous carbon spheres/carbon nanotubes as high-performance lithium storage materials. *Chem. Eng. J.* **2019**, *370*, 89−97.
(69) Sahoo, S.; Naik, K. K.; Late, D. J.; Rout, C. S. Electrochemical synthesis of a ternary transition metal sulfide nanosheets on nickel foam and energy storage application. *J. Alloys Compd.* **2017**, *695*, 154−161.
(70) Lu, Y.; Liu, X.; Wang, W.; Cheng, J.; Yan, H.; Tang, C.; Kim, J.; Luo, Y. Hierarchical, porous CuS microspheres integrated with carbon nanotubes for high-performance supercapacitors. *Sci. Rep.* **2015**, *5*, No. 16584.
(71) Karade, S. S.; Banerjee, K.; Majumder, S.; et al. Novel application of non-aqueous chemical bath deposited Sb_2S_3 thin films as supercapacitive electrode. *Int. J. Hydrogen Energy* **2016**, *46*, 21278−21285.
(72) Wen, X.; Zhang, H. Photoelectrochemical properties of $CuSGeO_2$-TiO_2 composite coating electrode. *PLoS One* **2016**, *11*, No. e0152862.
(73) Basu, M.; Nazir, R.; Fageria, P.; Pande, S. Construction of CuS/Au heterostructure through a simple photoreduction route for enhanced electrochemical hydrogen evolution and photocatalysis. *Sci. Rep.* **2016**, *6*, No. 34738.
(74) Li, W.; Yang, J.; Jiang, Q.; Luo, Y.; Hou, Y.; Zhou, S.; Xiao, Y.; Fu, L.; Zhou, Z. Electrochemical atomic layer deposition of Bi_2S_3/Sb_2S_3 quantum dots co-sensitized TiO_2 nanorods solar cells. *J. Power Sources* **2016**, *307*, 690−696.
(75) Camara, S. M.; Wang, L.; Zhang, X. Easy hydrothermal preparation of Cu_2ZnSnS_4 (CZTCS) nanoparticles for solar cell application. *Nanotechnology* **2013**, *24*, No. 495401.
(76) Hussain, A.; Rahman, A. Electrical and photovoltaic characteristics of Ni/(n)Bi_2S_3 Schottky barrier junction. *Superlattices Microstruct.* **2015**, *80*, 39−52.
(77) Meng, X.; Xu, Z.; Wang, M.; Yin, H.; Ai, S. Electrochemical behavior of antipyrine at a Bi_2S_3 modified glassy carbon electrode and its determination in pharmaceutical formulations. *Anal. Methods* **2012**, *4*, 1736−1741.
(78) Huang, G.; Zhang, J.; Jiang, F.; Zhang, Z.; Zeng, J.; Qi, X.; et al. Chemistry excellent photoelectrochemical activity of Bi_2S_3 nanorod/TiO_2 nanoplate composites with dominant {001} facets. *J. Solid State Chem.* **2020**, *281*, No. 121041.
(79) Castro, J. R.; Molloy, K. C.; Liu, Y.; Lai, S.; Dong, Z.; White, J.; Tiekink, E. R. T. Formation of antimony sulfide powders and thin films from single-source antimony precursors. *J. Mater. Chem.* **2008**, *18*, 5399−5405.

https://doi.org/10.1021/acsomega.1c02249
ACS Omega 2021, 6, 18975−18987